Journal of Materials Chemistry A

ROYAL SOCIETY OF CHEMISTRY

PAPER

View Article Online
View Journal | View Issue

Check for updates

Cite this: J. Mater. Chem. A, 2025, 13, 20725

Bimetallic Mg/Zn-based zeolitic imidazolate frameworks for zinc–air batteries: disclosing the role of defective imidazole-Mg sites in the electrocatalytic performance†

Valentín García-Caballero, [a] José A. Salatti-Dorado, [a] Luis Camacho, [a] Manuel Cano, *[a] Antonio J. Fernández Romero, [ab] Juan J. Giner-Casares [a] and Carolina Carrillo-Carrión *[c]

Received 6th January 2025
Accepted 20th May 2025

DOI: 10.1039/d5ta00123d

rsc.li/materials-a

The development of new noble metal-free, non-toxic and low-cost materials with efficient catalytic properties for the oxygen reduction reaction (ORR) is a key issue for improving energy storage devices, such as fuel cells or metal–air batteries. Herein, taking inspiration from the function of Mg in nature as a cofactor in many catalytic reactions, we have synthesized bimetallic Mg/Zn-based zeolitic imidazolate frameworks (Mg-doped ZIF-8), which resulted in a significant improvement in the electrocatalytic activity for ORR compared to pristine ZIF-8, especially when prepared as nanosized rather than microsized particles. Under optimized synthetic conditions, we succeeded in incorporating a large amount of Mg within the ZIF-structure (17.5% mol Mg doping), which was critical for improving the ORR response. Importantly, this work demonstrates for the first time the role of Mg as a dopant in ZIFs to boost the ORR performance, revealing that di-coordinated imidazole-Mg species (Im_2Mg) are the key active sites that enhance the adsorption of O_2 and water in the ORR process, as evidenced by our computational studies. Exploiting the exceptional electrocatalytic performance of the as-prepared Mg-doped ZIF-8 nanoparticles, we built zinc–air batteries that exhibited a specific capacity of 4.95 A h g^{-1}, significantly surpassing the values reported previously for other catalysts containing single-atom M–N–C sites.

1. Introduction

Electrochemical energy conversion and storage (EECS) is an emerging field of energy technology, which applies electrochemistry for storing energy in chemical fuels and supplying electricity appropriately through reversible reactions. For instance, fuel cells, electrolyzers or photoelectrolyzers, batteries, and supercapacitors are some representative EECS devices, which play a key role in the advancement of electric vehicles, grid storage, portable devices, and other applications yet to be explored. The development of low-cost high-performance electrocatalysts is essential to the overall performance of all these devices.[1]

To date, Li-ion batteries (LIBs) are probably the most used energy storage devices.[2,3] Unfortunately, LIBs have several drawbacks, such as lithium (Li) is a critical raw material with limited global Li reserves, detrimental environmental impacts of Li extraction, LIBs generate hazardous waste when disposed of, and they carry a risk of fire or explosion due to failure or overheating. In this scenario, zinc–air batteries (ZABs) have emerged as a highly promising alternative, displaying a number of intrinsic advantages. For instance, ZABs contain a cheap and sustainable Zn-anode, which is an easily recyclable and biocompatible raw material. In addition, ZABs use non-toxic and non-flammable aqueous electrolyte, and oxygen from air as the cathodic active material, offering competitive values of energy density, specific capacity and power performance.[4] One of the major limitations of ZABs is the need for catalysts in the cathodic reaction for the oxygen electroreduction (ORR) to lower the overpotential value and to promote practical applications of these types of energy storage devices.[5] Pt-based materials are the benchmark electrocatalysts for the ORR. Unfortunately, the cost of this noble metal together with its limited earth-abundance are probably the major barriers to its commercial viability. For this reason, it is relatively urgent to design low-cost, efficient and stable non-precious metal-based

[a]Departamento de Química Física y Termodinámica Aplicada, Instituto Químico para la Energía y el Medioambiente (IQUEMA), Universidad de Córdoba, E-14014 Córdoba, Spain. E-mail: q82calum@uco.es

[b]Grupo de Materiales Avanzados para la Producción y Almacenamiento de Energía, Universidad Politécnica de Cartagena, Aulario II, Campus de Alfonso XIII, 30203 Cartagena, Spain

[c]Instituto de Investigaciones Quimicas (IIQ), CSIC-Universidad de Sevilla, 41092 Sevilla, Spain. E-mail: carolina.carrillo@csic.es

† Electronic supplementary information (ESI) available. See DOI: https://doi.org/10.1039/d5ta00123d

electrocatalysts for ORR to increase the catalytic efficiency and enable the development of green energy devices with good potential for translation to an industrial environment.

Among the different strategies for generating efficient and sustainable electrocatalyst materials with single-atom active sites, metal–organic frameworks (MOFs) have attracted much attention in recent years due to their structural diversity, easy tunability, and abundant accessible metal centres.[6–8] As a subfamily of MOFs, zeolitic imidazolate frameworks (ZIFs), constructed from tetrahedrally coordinated transition metal (M) ions linked by imidazole (Im) units, have been widely studied in electrocatalytic applications,[9–11] because of its high porosity, high chemical and thermal stability, easy and scalable preparation, and the possibility of incorporating different electrochemically active metal ions alone or in combination (Zn/Co, Zn/Mn).[12–14] Notably, the unique structure of ZIFs allows for multiple metal–nitrogen coordination units ($M–N_4$; M = Zn, Co, Cu), which have been widely demonstrated to be very effective electroactive sites. However, in most of these studies, the ZIF is simply used as a sacrificial template to prepare N-doped porous carbon materials after a carbonization step, thus losing the intrinsic well-ordered structure of ZIFs. In general, when MOFs are subjected to high temperatures for carbonization/pyrolysis, they are likely to suffer from (i) collapse of the pore network, (ii) aggregation of particles with a consequent decrease in the accessible surface area, and (iii) poor batch-to-batch reproducibility since the carbonization process is quite difficult to control precisely.[15] To avoid these issues, the design of MOFs with good electrocatalytic response in their pristine form (*i.e.*, well-defined structure, with homogeneous catalytic sites, and regular and controlled porosity) is essential. To date, only a few studies have exploited pristine MOFs as electrocatalysts,[16–20] clearly indicating that it is still challenging to prepare high-quality MOF particles (*i.e.*, precise structural control with abundant accessible active sites) endowed with good electrocatalytic activity.

Taking inspiration from biochemical reaction of enzymes, Liu and co-workers recently proposed the incorporation of atomically dispersed magnesium (Mg) within a graphene framework, demonstrating that N-coordinated Mg cations exhibited high oxophilicity due to an elevated p-band centre position compared to other coordination environments, transforming the main-group element Mg into a highly active electrocatalyst for the ORR.[21] This idea was based on enzymes that use Mg as a cofactor, which are extremely active in biochemical reactions. For instance, more than 300 enzymes require Mg ions for their catalytic action, including all enzymes using or synthesizing ATP, and those that use other nucleotides to synthesize DNA and RNA.[22] Other representative example in the nature is the presence of Mg as single atoms in chlorophyll molecules, playing a key role in photosynthesis reactions.[23]

With the aim of combining the advantages of ZIFs, their well-defined porous architecture containing $M–N_4$ sites, with the potential of Mg as an active ORR element as well as its other beneficial properties such as its biocompatible nature and its abundance in the Earth's crust,[21] we set out to synthetize Mg-doped ZIF-8 by using a one-pot simple, reproducible, and sustainable method; key issues in view of future industrial applications of these MOFs include minimizing the cost, use environmentally friendly conditions, and ensuring the scalability of the synthetic procedure. Unfortunately, according to the literature this does not seem to be a straightforward task as the tetrahedral Mg^{2+}–N coordination geometry is uncommon. Kitagawa and co-workers reported the successful preparation of Mg-ZIF-8 from $Mg(BH_4)_2$ as a precursor under an Ar atmosphere and using acetonitrile as a synthesis solvent.[24] Regrettably, in contrast to Zn-ZIF-8, the obtained Mg-ZIF-8 was very sensitive to humidity in air, resulting in immediate decomposition upon exposure to air, thus making it unsuitable for applications. Other attempts under different conditions, such as using anhydrous $MgCl_2$ as the salt precursor and another synthesis solvent (tetrahydrofuran), also failed to produce stable Mg-ZIF-8. Besides, the use of protic solvents (water and methanol), which are most commonly used in the synthesis of ZIFs, was not possible due to the reactivity of $Mg(BH_4)_2$. These results clearly highlight that finding the optimal synthetic conditions is critical to stabilising the tetrahedral Mg^{2+}–N coordination geometry.

In this work, several Mg-doped ZIF-8 materials have been synthesized under optimized conditions to enable the incorporation and stabilization of the Mg ions within the framework, and exhaustively characterized in order to investigate the maximum doping percentage that yields stable Mg-doped ZIF-8 particles, as well as the effect of doping percentage on the ORR electrochemical response. In addition, the influence of particle size of the Mg-doped ZIF-8 on ORR performance has been evaluated. Finally, the best Mg-doped ZIF-8 candidate was tested as an air electrode in a ZAB and compared against a benchmark 10% wt. Pt–C based electrode to investigate the actual potential of the designed MOF for the construction of ZABs.

2. Results and discussion

The synthetic process of the Mg-doped ZIF-8 particles is illustrated in Fig. 1, with the samples designated as $nZIFMg_X$ and $mZIFMg_X$ for the nanosized and microsized particles, respectively. In brief, the particles were fabricated using the coprecipitation method at RT in water as the synthesis solvent, and different ratios of Zn/Mg were used to yield Mg-doped ZIF-8 particles with increasing Mg doping percentages (X corresponds to the Mg mol% used in the synthesis). By controlling the experimental conditions (*i.e.*, the metal to MeIm ratio, metal salts used as precursors, and reaction time) and the presence or absence of the surfactant CTAB as a capping agent for controlling the crystal growth, we could prepare either nanosized or microsized particles of ZIF-8 containing Mg(II), which replaced some Zn(II). In principle, the smaller ionic radius of Mg^{2+} (0.72 Å) compared to Zn^{2+} (0.74 Å) favors the incorporation of Mg into the structure, ruling out potential steric hindrance. SEM images revealed that $mZIFMg_X$ (X = 0, 20) particles exhibited a rhombic dodecahedron shape with a size of *ca.* 1 μm, while the $nZIFMg_X$ (X = 0, 20) particles of *ca.* 120 nm had a cubic shape, as shown in Fig. 1. More representative SEM

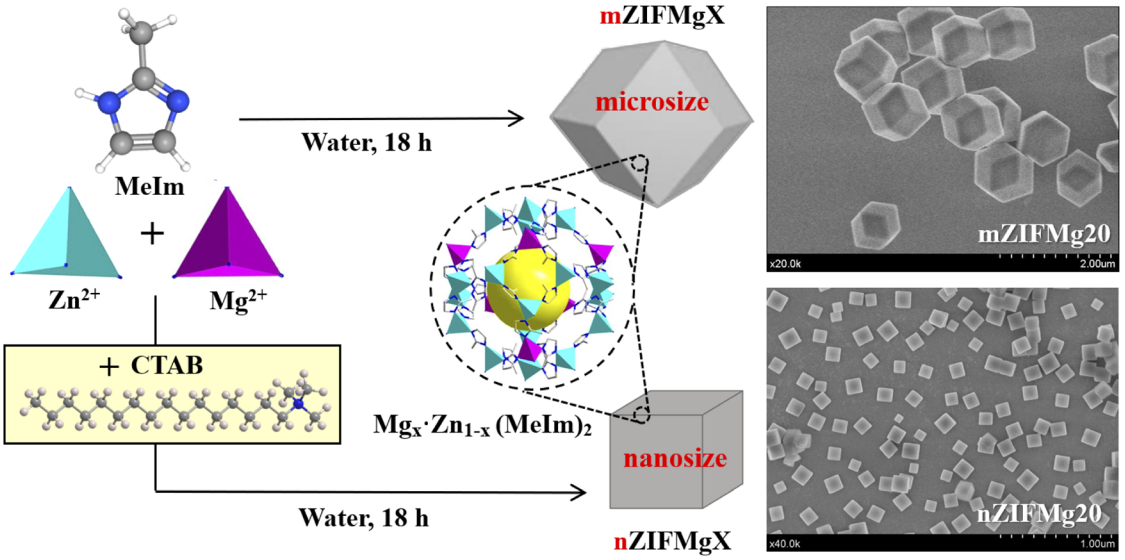

Fig. 1 Schematic illustration of the synthesis procedure of microsized mZIFMg$_X$ and nanosized nZIFMg$_X$ particles, including representative SEM images of the samples prepared with 20% mol Mg (nZIFMg$_{20}$ and mZIFMg$_{20}$).

images of samples with different Mg mol% are included in the ESI (Fig. S1).† EDX-SEM was routinely used to confirm the presence of Mg in the doped samples (Fig. S2†). The change in crystal morphology in the presence of CTAB is due to the fact that the CTAB molecules are adsorbed more strongly on {100} faces of ZIF-8 than on other faces, due to the higher hydrophobicity of the {100} faces, thereby leading to a decrease in the growth rate on those faces.[25] Our results showed that the substitution of some Mg(II) ions for Zn(II) ions does not modify the effect of CTAB, as it has also been observed in the case of replacing Co(II) by Zn(II) ions.[26,27] However, the addition of Mg(II) ions did significantly affect the kinetics of crystal formation; specifically, it slowed down the kinetics of the crystal growth, which was observable with the naked eye through the change in the turbidity of the reaction mixture with time.

To investigate in more detail the doping reaction mechanism, we used 5 different initial Mg percentages in the preparation of the nZIFMg$_X$ series (5, 20, 50, 70, and 100%). Notably, when the percentage of Mg was greater than 50% we did not obtain any solid even after increasing the reaction time to 48 h, which indicates that the Mg–MeIm coordination is less favourable, or at least less stable, than the Zn–MeIm coordination. This agrees with a previous study[27] that estimated the lattice formation energies of Zn-ZIF-8 and Mg-ZIF-8 using *ab initio* calculations, revealing that the energy of the coordination bond of Mg^{2+}–N in Mg-ZIF-8 is 138 kJ mol^{-1} lower than that of Zn^{2+}–N in Zn-ZIF-8, which evidences the substantial thermodynamic instability of Mg–MeIm. Furthermore, we again observed that the higher the percentage of Mg added, the slower the particle growth rate, resulting in smaller nanoparticles if the synthesis was stopped at short times (*ca.* 2–3 h). However, when the reaction time was prolonged (overnight, 18 h), the final sizes of the particles showed very little difference, as shown by SEM images (Fig. S1†) and, more exhaustively, by the comparison of the hydrodynamic sizes of the particles in solution, as determined by DLS (Fig. 2A and Table S1†). EDX-SEM clearly showed the presence of Mg after doping (Fig. S2†). Regardless of the particle size, Mg was uniformly distributed within the particles, as demonstrated by EDX-STEM elemental mapping analysis (Fig. S3 and S4†). Next, we studied the crystallinity of the prepared particles by PXRD. As shown in Fig. 2B, all the samples showed the typical diffraction peaks of the sodalite structure of ZIF-8.[28] This is a cubic structure with space group $I\bar{4}_3m$ (no. 217) and a network size of 17.012 Å. All peaks exhibited high intensity and narrow width, even in the nanosized particles, which is indicative of a high degree of crystallinity in the samples. No additional peaks were found in the Mg-doped samples compared to the control ones (nZIFMg$_0$ and mZIFMg$_0$) and the simulated ZIF-8 pattern, confirming that the incorporation of different amounts of Mg to replace Zn does not affect the crystalline structure of pristine ZIF-8.

Afterwards, we determined the actual amount of Mg incorporated in the samples by digesting them with aqua regia and subsequent analysis by ICP-OES. Fig. 2C shows the actual Mg incorporated (Mg found, mol%) compared to the theoretical amount added during synthesis (Mg added, mol%); values are given in Table S2.† Surprisingly, these values were significantly lower than expected, further indicating that the coordination of Mg with the MeIm ligands is much less favourable than that of Zn, and the maximum doping percentages were 17.5 and 12.6% for the nanosized and microsized particles, respectively. It was not possible to achieve higher Mg doping with the same synthetic procedure, since increasing the ratio of Mg to Zn in the reaction mixture inhibited the formation of crystals as mentioned above. In an attempt to increase the amount of Mg incorporated into the structure, we carried out the synthesis of mZIFMg$_{20}$ in methanol. Surprisingly, we found that the Mg doping was almost negligible, at only 2.8%, which clearly

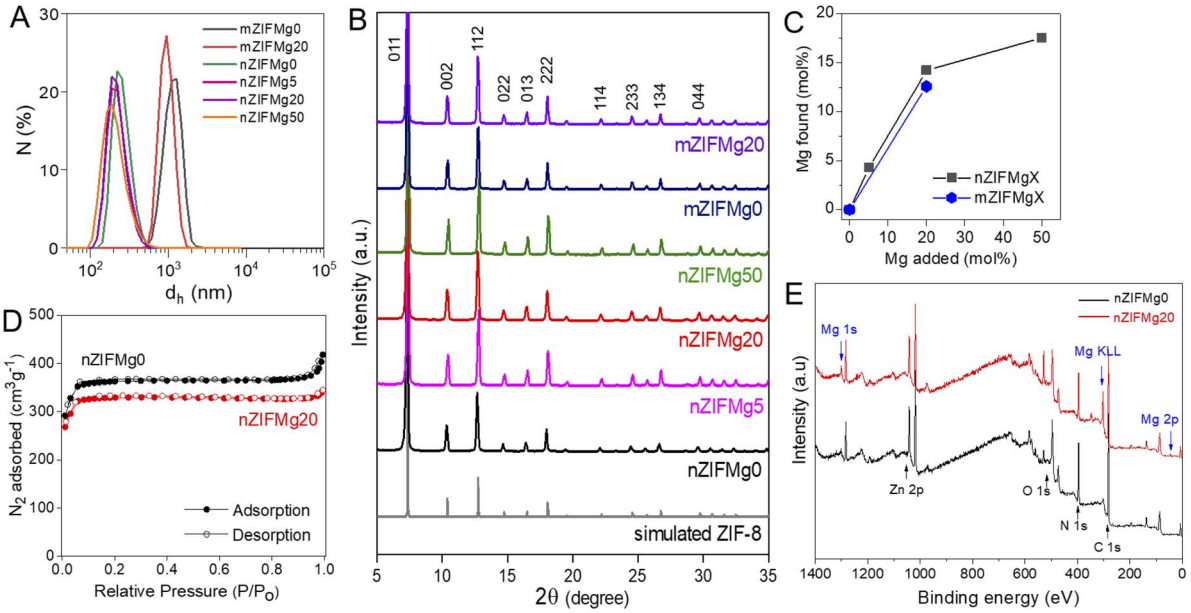

Fig. 2 (A) DLS number (N) distributions of the hydrodynamic diameter d_h for the as-prepared nanosized (nZIFMg$_X$; X = 0, 5, 20, 50) and microsized (mZIFMg$_X$; X = 0, 20) particles dispersed in methanol. (B) PXRD patterns of the different samples, showing the crystalline planes; the simulated ZIF-8 pattern (black, COD: 7111970) is included for comparison. (C) Plot of the actual Mg incorporated *versus* the added values (expressed in mol%) in the different samples as determined by ICP-OES. (D) N_2 isotherms (77 K) of the nanosized nZIFMg$_0$ and nZIFMg$_{20}$ particles. Closed symbols represent adsorption, and empty symbols represent desorption. (E) XPS survey spectra of the nanosized nZIFMg$_0$ and nZIFMg$_{20}$ particles.

reveals the key role played by water as solvent in the synthesis for the stabilization of the tetrahedral coordination of Mg ions (Mg–N_4). As previously reported, the solvent plays an active role in the synthesis of ZIF-8 by influencing the crystallization rate, crystal size and morphology, crystallinity, and metal coordination.[29–32] In methanol, ZIF-8 crystallizes extremely rapidly, typically within 1–2 minutes. This ultra-fast crystallization significantly limits the incorporation of dopant metals with lower coordination energies than Zn, such as Mg, into the framework. In contrast, the growth rate in water is substantially slower, with turbidity typically appearing only after 1–2 hours, depending on the Mg mol%. This slower process provides enough time for Mg ions to coordinate with the imidazole linker. Additionally, the higher hydrogen bond donation (HBD) capacity of water compared to methanol likely enhances the polarization of the pyrimidinic hydrogen on the imidazole linker, facilitating its deprotonation and subsequent coordination with metal cations (*i.e.*, M–MeIm–M complexes; M = Zn or Mg). This behavior supports the reaction progression at the high linker concentrations used in this work. The superior HBD ability of water may also compensate for the lower thermodynamic stability of Mg^{2+}–N bonds in Mg-doped ZIF-8, leading to more efficient Mg incorporation when the synthesis is carried out in water. In other words, the favorable Mg–water interaction[33] may enhance Mg ion accessibility to the deprotonated linker molecules, where water molecules, acting as ligands, can provide a growth template and facilitate further ZIF-8 crystal growth.

To evaluate whether the beneficial role of water as a solvent in enhancing metal doping levels could be extended to other metal cations, we applied the same synthetic procedure using either Fe(II) or Cu(II) as dopant cations, with methanol or water as solvents. Interestingly, in all cases, higher doping percentages were achieved when the synthesis was carried out in water, as determined by ICP-OES (Table S3†). The values obtained from the methanol-based synthesis were consistent with those reported in the literature,[34,35] with maximum doping percentages remaining relatively low (<5%). Importantly, under our optimized water-based synthesis conditions, we achieved 17.5% Mg doping in the nanosized particles, which is expected to be decisive in enhancing the ORR activity of pristine ZIF-8.

We also studied the effect of Mg doping on the textural properties of ZIF-8 by measuring the N_2 sorption isotherms of nanosized particles containing 0 and 20% Mg. As shown in Fig. 2D, both particles exhibited a reversible type I isotherm, typical for microporous materials. The Brunauer–Emmett–Teller (BET) surface area decreased slightly after Mg doping (S_{BET} = 1100 m^2 g^{-1}) compared to the non-doped ZIF-8 (S_{BET} = 1218 m^2 g^{-1}), in agreement with the results reported for Cu-doped ZIF-8,[36] and Cu/Fe-doped ZIF-8.[34] Nevertheless, the overall results indicate that the partial replacement of Zn by Mg ions within the framework did not significantly affect the porosity of the material in terms of micropore area and total pore volume (Table S4†). Fig. 2E compares the resulting XPS survey spectra of nZIFMg$_0$ and nZIFMg$_{20}$ particles, where the presence of Mg in the latter case can be observed with two characteristic peaks at *ca.* 303 and 47 eV (Fig. S6B†), which can be assigned to Mg Auger and Mg 2p, respectively. In addition, three characteristic peaks of Zn were identified in both samples, at ~1021 eV, and at *ca.* 136 and 196 eV assigned to Zn 3p and Zn

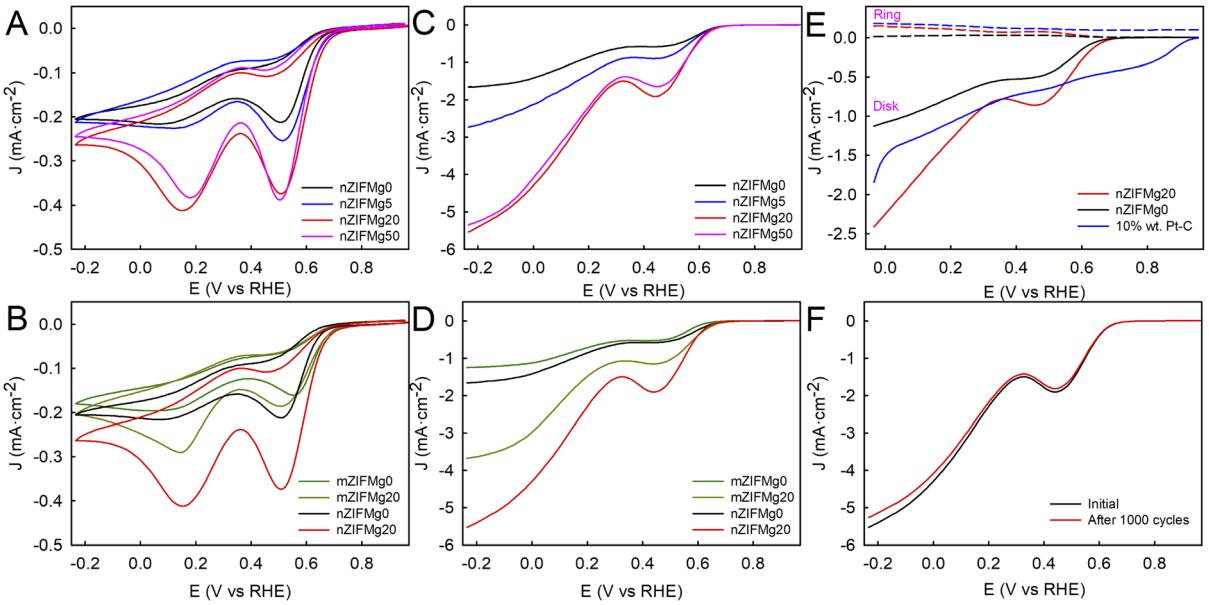

Fig. 3 (A and B) Cyclic voltammetry (CV) and (C and D) rotating disk voltammetry (RDV) curves recorded at a rotation rate of 2500 rpm for the different nanosized (nZIFMg$_0$, nZIFMg$_5$, nZIFMg$_{20}$, and nZIFMg$_{50}$) and microsized (mZIFMg$_0$, mZIFMg$_{20}$) Mg-doped samples. (E) Linear sweep voltammetry curves of RRDE modified with nZIFMg$_{20}$, nZIFMg$_0$ and 10% wt. Pt–C, using a rotation rate of 1600 rpm and keeping Au-ring at a constant potential of 1.4 V *vs.* RHE. (F) RDV curves of the GCE modified with nZIFMg$_{20}$ before and after 1000 cycles of the AAT, using a rotation rate of 2500 rpm. All measurements were performed in O_2-saturated 0.1 M KOH. Scan rates: 0.1 V s^{-1} for CV and 0.01 V s^{-1} for RDV and RRDE.

3s, respectively. Regarding the oxidation state of Zn and Mg ions in the particles, high resolution XPS Zn 2p and Mg 2p analyses were carried out for nZIFMg$_0$ and nZIFMg$_{20}$ samples (Fig. S5G and S5H†). On the one hand, the deconvoluted Zn 2p$_{3/2}$ core level XPS spectra showed similar single peaks, centred at *ca.* 1019 eV, attributed to the presence of Zn(II).[37] And on the other hand, Fig. S6† shows the resulting Mg 2p core level XPS spectrum for nZIFMg$_{20}$, which shows a single peak at *ca.* 47 eV, attributed to the electronic state 2p$_{1/2}$ of Mg ions in the +2-oxidation state.[38] In addition, HR C 1s, O 1s, and N 1s XPS spectra of nZIFMg$_0$ and nZIFMg$_{20}$ were almost identical (Fig. S5†), further confirming that the partial replacement of Zn by Mg ions within the framework did not affect the chemical composition and oxidation states of the other elements. It is worth noting that a higher amount of O_2 was observed for nZIFMg$_{20}$ compared to nZIFMg$_0$, as can be seen in Fig. S6A† where the intensity of the O_2 peak in both samples is compared.

Once characterized, the electrocatalytic performance of the Mg-doped ZIF-8 particles for the ORR was investigated. Fig. S7† shows representative cyclic voltammograms (CVs) of GCEs modified with nZIFMg$_0$ and nZIFMg$_{20}$ in 0.1 M KOH electrolyte solution, under nitrogen- and oxygen-saturated conditions, respectively. The absence of any redox process under N_2-saturated conditions confirmed that the ORR catalysis occurred in the presence of O_2. Importantly, significant differences in the onset potential and in maximum current density values were observed, with nZIFMg$_{20}$ showing better catalytic properties for the ORR (0.71 V *vs.* RHE and −0.42 mA cm^{-2}) than nZIFMg$_0$ (0.66 V *vs.* RHE and −0.21 mA cm^{-2}), demonstrating the benefit of Mg doping in the ZIF-8 structure. When comparing the different Mg doping percentages (Fig. 3A), we found that the nZIFMg$_{20}$ sample, which contains 14.2 mol% Mg according to ICP analysis, exhibited the best electrocatalytic performance for the ORR. It is worth noting that a further increase in the amount of Mg to 17.5 mol% did not lead to an improvement in the response as observed for nZIFMg$_{50}$. A similar trend could be observed with RDV curves measured using a rotation rate of 2500 rpm (Fig. 3C). On the other hand, the particle size strongly affected the ORR activity, as shown in Fig. 3B and D under static and dynamic conditions, respectively. These results demonstrate that nanosized particles, either Mg-doped or undoped, showed a higher electrocatalytic response compared to their respective microsized counterparts. This finding has already been reported for other MOF-based catalysts,[39] and is attributed to the higher surface-to-volume ratio and shorter diffusion paths in nanosized MOFs, thus allowing easier accessibility to active sites located in the innermost pores. Furthermore, the electrochemical surface areas (ECSAs) of the nZIFMg$_0$ and nZIFMg$_{20}$ samples were determined by the double layer capacitance method.[16] Fig. S8A and S8B† show the typical CV curves obtained in the non-faradaic region for both samples at various scan rates (from 20 to 100 mV s^{-1}), while Fig. S8C† plots the difference in current density between the anodic and cathodic sweeps (ΔJ) against the scan rates. The double-layer capacitance (C_{dl}) was calculated using the equation $C_{dl} = \Delta J/2$, obtaining values of 13.6 and 33.2 μF cm^{-2} for nZIFMg$_0$ and nZIFMg$_{20}$, respectively. These results clearly demonstrate that nZIFMg$_{20}$ has a higher number of electrochemically active sites than nZIFMg$_0$. In addition, electrochemical impedance spectroscopy (EIS) was performed on both samples. The EIS data were fitted using the Randles equivalent circuit shown in Fig. S8D,† where R_1 represents the solution resistance, R_2 represents the charge-transfer resistance, Q_1 is the double-layer capacitance at the electrode surface, and W_1 is the Warburg resistance. The

extracted parameters are listed in Table S6† for both samples. Overall, the lower R_2 value and higher Q_1 value for nZIFMg$_{20}$ indicate enhanced electron transfer compared to nZIFMg$_0$.

Next, RRDE analysis was performed for nZIFMg$_0$, nZIFMg$_{20}$ and 10% wt. Pt–C to compare the ORR kinetics. Fig. 3E shows the resulting linear sweep voltammetry curves in O_2-saturated 0.1 M KOH, using a rotation rate of 1600 rpm and keeping the Au ring at a constant potential of 1.4 V *vs.* RHE. Although the electrode modified with 10% wt. Pt–C displayed a higher onset potential, notably the one modified with nZIFMg$_{20}$ exhibited a higher maximum current density with a value of −2.61 mA cm^{-2} compared to −1.84 mA cm^{-2} for the standard/reference 10% wt. Pt–C catalyst. Additionally, the number of electrons transferred per O_2 molecule, and the percentage of peroxide produced for each material were calculated (see the ESI for details, Table S5†), showing a dominant four-electron pathways and quite low percentages of peroxide produced (<1%) in all cases.

The long-term stability of nZIFMg$_{20}$ as an ORR electrocatalyst was investigated using an accelerated aging test (AAT), which consisted of 1000 continuous potential cycles performed by CV measurements in O_2-saturated 0.1 M KOH solution.[16] Importantly, only a slight decrease in current density was observed after 1000 cycles (Fig. 3F), which can be associated with the loss of material deposited on the GCE surface during the AAT. This study confirms the good stability of nZIFMg$_{20}$ under working conditions in alkaline electrolytes, which is a relevant aspect for future industrial applications of these materials.

In order to investigate the reason behind the improved electrochemical performance of the nanosized Mg-doped ZIF-8 compared to pristine ZIF-8, we carried out computational studies. It is important to highlight that the catalytic activity of ZIF-8 has been primarily attributed to unsaturated coordination sites, where metal ions or ligands are exposed with incomplete coordination, rather than to the fully tetrahedrally coordinated metal nodes.[40,41] Experimental evidence supporting the link between catalytic activity and surface defects includes the superior performance of nanosized nZIFMg$_X$ particles compared to their microsized mZIFMg$_X$ counterparts. This is likely due to the higher specific surface area of the nanoparticles, which results in a greater density of low-coordination sites. Although alternative scenarios were also considered to explain the effect of Mg doping, computational studies ruled out those possibilities (see the ESI† for details). Therefore, we modelled the ZIF-8 and Mg-doped ZIF-8 structures by incorporating surface defects, that is Zn or Mg ions with lower coordination (Fig. 4A, see details in the Experimental section). Fig. 4A(1) shows the appropriate cutting plane (indicated with a red line) to generate Zn atoms bound to only two ligands (Im_2Zn) on the exposed surface. Likewise, another cutting plane (indicated with a black line) was used to generate Zn atoms coordinated with 3 ligands (Im_3Zn) on the surface. From this structure, cut-out surfaces have been constructed along the face (110), as shown in Fig. 4A(2). The option of generating cutting planes that expose Zn atoms bound to a single ligand (ImZn) was not considered, due to the low probability of such configurations occurring at room temperature and atmospheric pressure as previously reported.[38] Next, the 2D structures constructed using the previous procedure were transformed into 3D structures, incorporating an empty region to achieve a thickness of 25 Å. Therefore, the final unit cell dimensions are 17.012 Å × 24.058 Å × 25 Å, and the stoichiometry is $C_{96}H_{120}N_{48}Zn_{12}$. Using this procedure, structures were constructed in which only 4 Zn atoms per unit cell are exposed on the surface, either in the Im_2Zn or Im_3Zn form. While for the construction of the Im_2Mg and Im_3Mg systems, 25% of the Zn atoms on the surface (1 of each 4) were replaced by Mg, keeping the internal Zn atoms unchanged.

On the one hand, considering that the catalytic activity of ZIF-8 originates mainly from unsaturated coordination sites, the better electrochemical response obtained with both the pristine ZIF-8 and Mg-doped ZIF-8 at the nanoscale compared to their respective microsize counterparts is explained by the increased number of defects present in nanosized ZIF-8 particles.[42] On the other hand, to explain the differences observed in the absence or presence of Mg ions, we carefully studied the mechanism of the ORR process using the method developed by Nørskov *et al.*[43] In an alkaline medium, H_2O instead of H_3O^+ can act as a proton donor, *i.e.* $O_2 + 2H_2O + 4e^- \leftrightarrow 4OH^-$. Given the incomplete coordination of the metal, it was assumed that the entire process takes place through adsorbed species, thus incorporating the adsorptions of O_2 and H_2O into the model. Therefore, the 4 elementary steps that describe the mechanism were as follows:

$$MO_2 + H_2O(l) + e^- \leftrightarrow MOOH + OH^- \quad (1)$$

$$MOOH + e^- \leftrightarrow MO + OH^- \quad (2)$$

$$MO + H_2O(l) + e^- \leftrightarrow MOH + OH^- \quad (3)$$

$$MOH + H_2O(l) + e^- \leftrightarrow MH_2O + OH^- \quad (4)$$

The exchange reaction was incorporated into these elementary steps:

$$MH_2O + H_2O(l) \leftrightarrow MO_2 + 2H_2(g) \quad (5)$$

where M represents Im_3Zn, Im_3Mg, Im_2Zn or Im_2Mg. The absorption free energies of each component were obtained from the following relationships:

$$M + 2H_2O(g) \leftrightarrow MO_2 + 2H_2(g) \quad \Delta G_{MO_2}$$

$$M + 2H_2O(g) \leftrightarrow MOOH + (3/2)H_2(g) \quad \Delta G_{MOOH}$$

$$M + H_2O(g) \leftrightarrow MO + H_2(g) \quad \Delta G_{MO}$$

$$M + H_2O(g) \leftrightarrow MOH + (1/2)H_2(g) \quad \Delta G_{MOH}$$

$$M + H_2O(g) \leftrightarrow MH_2O \quad \Delta G_{MH_2O}$$

The free energy variations for steps (1)–(5) were calculated from the following relations:

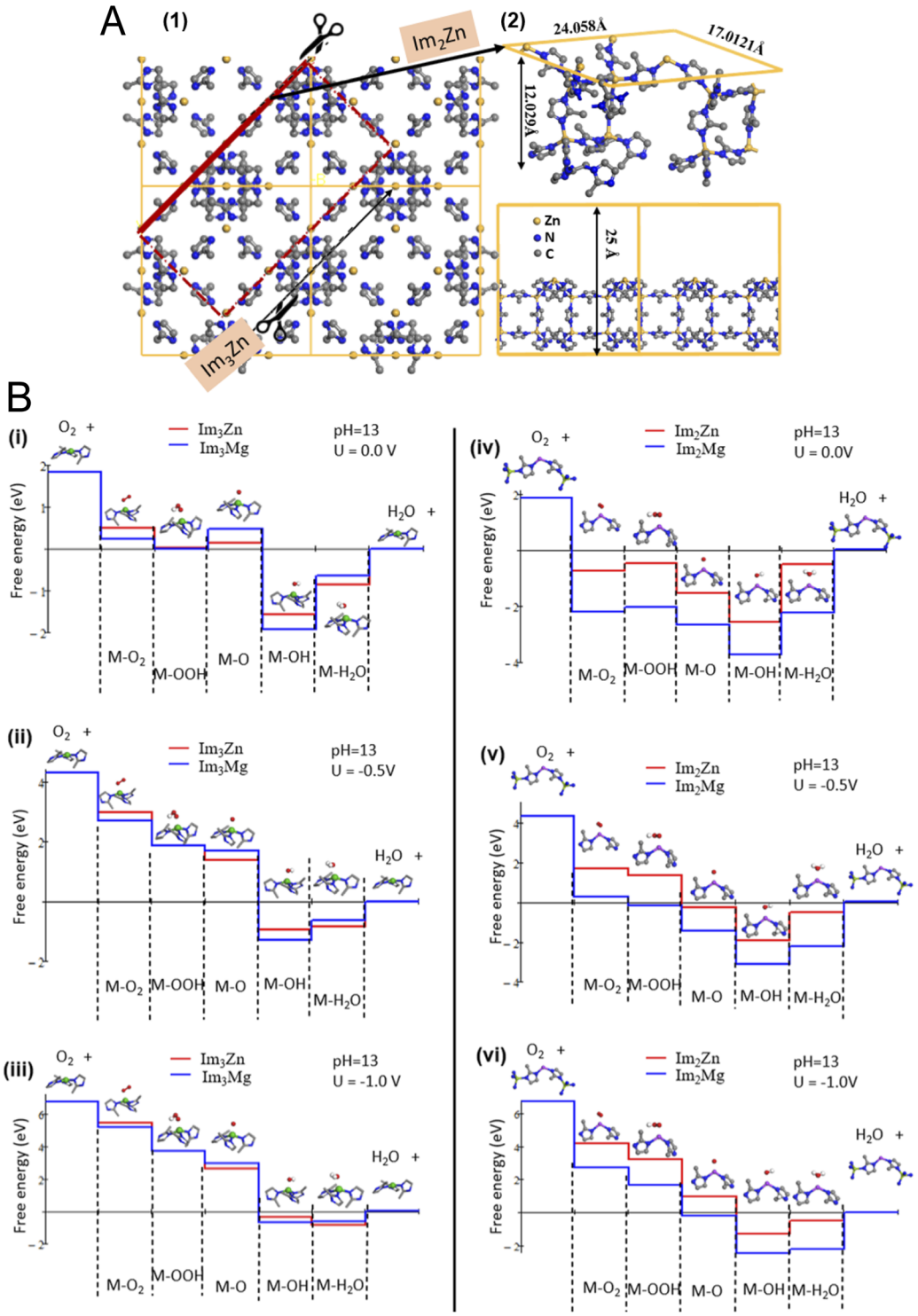

Fig. 4 (A) Constructed structures based on ZIF-8 for our computational studies. (1 and 2) Cut-out surfaces constructed along the face (110), and the resulting 3D structure obtained from the 2D one, but including an empty region until completing a thickness of 25 Å. Note that for the Mg-doped ZIF-8, the same structures were constructed by replacing 25% of the Zn atoms on the surface (1 of each 4) with Mg, while keeping the internal Zn atoms unchanged. (B) Free-energy diagrams for ORR elementary steps on (i–iii) Im_3Zn and Im_3Mg at different electrode potentials U, and (iv–vi) Im_2Zn and Im_2Mg at different electrode potentials U (pH = 13).

$$\Delta G_1 = \Delta G_{MOOH} - \Delta G_{MO_2}$$

$$\Delta G_2 = \Delta G_{MO} - \Delta G_{MOOH}$$

$$\Delta G_3 = \Delta G_{MOH} - \Delta G_{MO}$$

$$\Delta G_4 = \Delta G_{MH_2O} - \Delta G_{MOH}$$

$$\Delta G_5 = \Delta G_{MO_2} - \Delta G_{MH_2O} - 4.92$$

In this model, the reversible hydrogen electrode RHE was selected as the reference electrode, which allowed us to replace the chemical potential (μ) of the proton–electron pair with that of the hydrogen molecule divided by two ($\mu_{H+} + \mu_{e-} = 1/2\mu_{H_2}$) for potential $U = 0$ V, pH = 0 and $P = 1$ bar. For non-zero potentials, $\Delta U = -neU$, where U is the applied potential relative to the RHE and for pH different from zero, $\Delta G_{pH} = kT\ln(10)$pH. Likewise, the following the relationship was used for the energy of O_2 formation:

$$G_{O_2} = 4.92\ \text{eV} - 2G_{H_2(g)} + 2G_{H_2O(l)}$$

The resulting ΔG values calculated using DFT without considering the effects of potential and at pH = 0 are shown in Table S7.† The difference between ΔG_{MOOH} and ΔG_{MOH} is 3.3 ± 0.3 eV, which is in consonance with previously reported values for transition metal-based catalysts.[44,45] While the resulting ΔG values calculated under different potentials (0.0, −0.5 and −1.0 V) at pH 13 are presented in Tables S8–S10.†

Fig. 4B(i–iii) compares the resulting variation in free energies for Im_3Zn and Im_3Mg, demonstrating that the determining stage was the formation of Im_3M–O, both with Zn and with Mg. The comparison of Im_2Zn and Im_2Mg, shown in Fig. 4B(iv–vi), led to similar mechanisms for Zn and Mg species.

As expected, the decrease in the number of Im ligands implies a decrease in the adsorption free energy in all cases. However, the main difference observed was a great decrease in free energy in the adsorption of O_2 and water in the case of Im_2Mg compared to Im_2Zn, as shown in Fig. 4B(iv–vi). This favorable adsorption of O_2 and water at Im_2Mg sites was observed regardless of the electrode potential used but was more significative at 0 V. This result is consistent with the improvement in the ORR catalytic behavior of the Mg-doped ZIF-8, as has already been found experimentally by voltametric analysis (Fig. 3).

Furthermore, based on the DFT results, we could attribute the superior catalytic properties of $nZIFMg_{20}$ to the more efficient adsorption of O_2 and water molecules on Im_2Mg than on Im_2Zn. In this regard, it is important to note that the more intense O 1s peak obtained for $nZIFMg_{20}$ (Fig. S6B†) further confirms the enhanced adsorption of O_2 and H_2O on Mg-doped ZIF8. Besides, the higher specific area of the nanosized $nZIFMg_{20}$ or $nZIFMg_0$, favors a greater number of Im_2Mg or Im_2Zn defects with respect to their microsized counterparts, thus increasing the catalytic activity of the nanosized particles. It should be noted that the enhanced adsorption of O_2 and H_2O on $nZIFMg_{20}$ occurs despite the fact that the BET surface area of Mg-doped ZIF-8 is slightly lower than that of pristine ZIF-8 ($nZIFMg_0$), as shown in Table S3.† This suggests that the increased adsorption of O_2 must be related to subtle structural changes induced by the partial substitution of Zn^{2+} with Mg^{2+} ions. One possible explanation lies in the altered flexibility of the MOF framework upon gas adsoprtion. This structural flexibility, attributed to the swinging motion of the imidazolate linkers, may facilitate the adsorption of molecules that are otherwise too large to pass through the narrow pore windows.[46,47] Another plausible explanation is related to the higher ionic character of the Mg^{2+}–N bond compared to the Zn^{2+}–N,[24] which influences the electronic density distribution and, therefore, it may determine the mode of adsorption of O_2, adsorption energy, and/or dissociation energy, ultimately affecting the ORR catalytic activity.

To further demonstrate the excellent cathodic features of $nZIFMg_{20}$ (*i.e.*, nanosized particles containing 14.2 mol% Mg) for O_2 transport in ORR, a flooded ZAB was built to investigate its possible application in a real device. During operation, the attainment of high-power density in ZABs relies on the establishment of adequate three-phase boundaries involving the electrolyte, ORR catalyst, and O_2 from air.[16,48,49] Hence, the O_2 supply from the air electrode is crucial to enable the formation of abundant liquid/solid/gas interfaces, essential for efficient power generation. $nZIFMg_0$, $nZIFMg_{20}$ and 10% wt. Pt–C were tested as the positive electrodes, using the same amount of catalyst (0.675 mg), with a Zn plate as the anode and KOH (6 M) as the liquid electrolyte. Fig. 5A shows the galvanostatic discharge for $nZIFMg_{20}$ at different intensities (first from 1 mA to 20 mA, and later from 20 mA to 1 mA), confirming the remarkable stability of this material as a cathode in ZABs. The potential values obtained demonstrated not only the stability of $nZIFMg_{20}$ but also the excellent battery performance recovery.

Fig. 5B and C compare the resulting polarization and power density curves for $nZIFMg_0$, $nZIFMg_{20}$ and 10% wt. Pt–C as air electrodes in ZAB, confirming that $nZIFMg_{20}$ provided higher

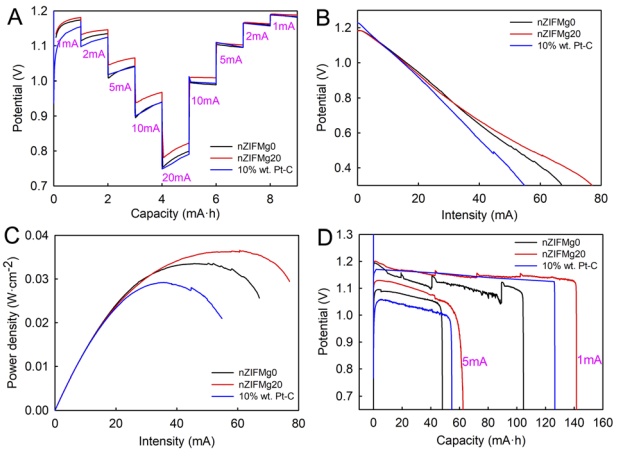

Fig. 5 (A) Representative short-term galvanostatic discharge curves at different intensities, (B) polarization curves, (C) power density plot, and (D) long-term galvanostatic discharge curves at −1 and −5 mA for $nZIFMg_0$, $nZIFMg_{20}$ and 10% wt. Pt–C, respectively.

Table 1 Specific capacity values obtained for ZABs based on $nZIFMg_0$, $nZIFMg_{20}$ and 10% wt. Pt–C

	Specific capacity (A h g^{-1})		
Intensity (mA)	$nZIFMg_0$	$nZIFMg_{20}$	10% wt. Pt–C
−5	1.67	2.17	1.89
−1	3.66	4.95	4.41

potential and maximum power density values than 10% wt. Pt–C. A maximum power density of 36.1 mW cm^{-2} at 53.4 mA was obtained for the battery with an air electrode containing 0.675 mg of $nZIFMg_{20}$, which revealed an excellent specific power density value of 53.5 kW cm^{-2} kg^{-1} (considering only the catalyst mass) or 0.58 kW cm^{-2} kg^{-1} (taking into account the mass of the entire air electrode, carbon paper + catalyst). It should be noted that the battery using 10% wt. Pt–C as the catalyst achieved a maximum power density of 29.1 mW cm^{-2} at 34.9 mA, and considering that 0.675 mg of Pt was added to the air electrode, the specific power density for this Pt–C air electrode was 43.1 kW cm^{-2} kg^{-1} (*i.e.* considering only the catalyst mass), which is 20% less than that obtained with $nZIFMg_{20}$.

Interestingly, a comparative study of the maximum discharge capacity at −5 mA for $nZIFMg_0$, $nZIFMg_{20}$ and 10% wt. Pt–C as air electrodes (Fig. 5D) showed that $nZIFMg_{20}$ exhibited a higher voltage and a lower potential loss than 10% wt. Pt–C. In addition, the maximum discharge capacity values were achieved with $nZIFMg_{20}$, which were significantly greater than those obtained with 10% wt. Pt–C both at −1 and −5 mA (Table 1). These values significantly exceed the specific capacities reported previously for others carbon-based catalysts containing $M–N_4$ single sites,[49] which clearly demonstrates the outstanding efficiency of $nZIFMg_{20}$ as a cathode in primary ZABs. It should be noted that the interaction between $nZIFMg_{20}$ and the GDL provides an enhanced catalyst–support interaction, significantly promoting the activity of the catalytic active sites and demonstrating that the choice of carbon-based electrode material strongly influences the resulting electrocatalytic performance.

Finally, a galvanostatic discharge of $nZIFMg_{20}$ into a flooded ZAB was performed at a high current of −10 mA, and the corresponding XPS post-characterization is shown in Fig. S9.† Overall, a comparison of the survey XPS spectra of $nZIFMg_{20}$ before and after the ZAB discharge reveals the presence of fluoride (F 1s) from the Nafion used as the catalyst-coated membrane, as well as a slight reduction in the Zn 2p and Mg 2p peaks, which is attributed to the additional Nafion layer. In addition, the HR-XPS spectra of Zn 2p and of Mg 2p showed that the oxidation states of zinc and magnesium remained unchanged after the ZAB discharge, with only a slight shift towards higher binding energies (Fig S8C†). Notably, an increase in the intensity of the HR-XPS O 1s was observed, which can be attributed to adsorbed O_2 during the ORR process under ZAB discharge conditions. Taken together, these results highlight the excellent ZAB performance of $nZIFMg_{20}$, a MOF material synthesized without calcination (*i.e.*, retaining its pristine porous and crystalline structure).

3. Experimental

3.1. Chemicals

All the reagents including 2-methylimidazole (MeIm), zinc nitrate hexahydrate ($Zn(NO_3)_2 \cdot 6H_2O$), zinc acetate dihydrate ($Zn(OAc)_2 \cdot 2H_2O$), magnesium nitrate hexahydrate ($Mg(NO_3)_2 \cdot 6H_2O$), magnesium acetate tetrahydrate ($Mg(OAc)_2 \cdot 4H_2O$), hexadecyltrimethylammonium bromide (CTAB), potassium hydroxide (KOH), Nafion and 10% wt. Pt–C were purchased from Merck and used as received without any purification.

3.2. Synthesis of nanosized Mg-doped ZIF-8 particles ($nZIFMg_X$)

Stock aqueous solutions of MeIm (1 M), $Zn(NO_3)_2$ (25 mM), $Mg(NO_3)_2$ (25 mM), and CTAB (1 mM) were prepared. 3 mL of MeIm solution was added under magnetic stirring at room temperature (RT) to 3 mL of a mixed solution of both metal salts (in different proportions according to the theoretical doping percentage, $X = 0$, 5, 20 and 50% Mg). After that, 3 mL of CTAB solution was added, and the mixture was stirred for 5 min and then left undisturbed overnight (18 h) at RT. The particles were then collected by centrifugation (10 000 RCF, 5 min), washed twice with methanol, and finally redispersed in methanol at a concentration of 15 mg mL^{-1}. These stock methanolic dispersions of the Mg-doped ZIF-8 nanoparticles (denoted as $nZIFMg_0$, $nZIFMg_5$, $nZIFMg_{20}$ and $mZIFMg_{50}$ for 0, 5, 20 and 50% mol of Mg added in the synthesis, respectively) were stored in a fridge until use.

3.3. Synthesis of microsized Mg-doped ZIF-8 particles ($mZIFMg_X$)

Stock aqueous solutions of MeIm (960 mM), $Zn(OAc)_2$ (60 mM), and $Mg(OAc)_2$ (60 mM) were prepared. 4 mL of MeIm solution was added under magnetic stirring at RT to 4 mL of a mixed solution of both metal salts (in different proportions according to the theoretical doping percentage, $X = 0$ and 20% Mg). The mixture was stirred for 5 min and then left undisturbed overnight (18 h) at RT. The particles were then collected by centrifugation (6000 RCF, 5 min), washed twice with methanol, and finally redispersed in methanol at a concentration of 15 mg mL^{-1}. These stock methanolic dispersions of the Mg-doped ZIF-8 microparticles (denoted as $mZIFMg_0$ and $mZIFMg_{20}$ for 0 and 20% mol of Mg added in the synthesis, respectively) were stored in a fridge until use.

3.4. Scale-up synthesis of Mg-doped ZIF-8

To evaluate the scalability of the synthesis methods, both nanosized and microsized Mg-doped ZIF-8 particles were prepared in large quantities by multiplying the volumes of the precursor's solutions by 10.

3.5. Characterization of materials

Scanning electron microscopy (SEM) images were acquired using a HITACHI S4800 field emission microscope operated at 2 kV in secondary electron and backscattered electron modes. Elemental composition was determined by Energy Dispersive X-ray analysis (EDX) using the same SEM instrument equipped with a Bruker-X Flash-4010 EDX detector, operated at 10 kV. A Talos F200i HR-TEM system, operated at an accelerating voltage of 80 kV, was used to record HR-TEM images and STEM-HAADF mode was employed to perform the mapping of the particles. The samples were prepared on 200 mesh copper grids coated with Formvar/carbon films. Powder X-ray diffraction (PXRD) analyses of the crystalline powder of samples were performed using X-ray radiation of Cu Kα on a Bruker D8-Advance diffractometer. Dynamic light scattering (DLS) measurements were carried out using a Malvern Zetasizer Nano ZSP equipped with a 10 mW He–Ne laser operating at a wavelength of 633 nm and fixed scattering angle of 173°. Inductively coupled plasma optical emission spectroscopy (ICP-OES) analyses were performed on an iCAP 7200 ICP-OES Duo (ThermoFisher Scientific) instrument. Prior to the measurement process to determine the Zn and Mg content, the particles were digested with aqua regia solution (3 : 1 nitric acid to hydrochloric acid) for 24 h at 80 °C. N_2 sorption isotherms (77 K) of powder samples were carried out in a Micromeritics Tristar II 3020 system. Before analysis, the samples were degassed under vacuum for 18 h at 120 °C. The apparent surface areas were calculated using the Barrett–Emmett–Teller (BET) method in the pressure interval P/P_o = 0.01–0.2 (with P_o being the saturation pressure). The pore volume and external surface area were calculated by the *t*-plot method. XPS studies were performed on an XPS SPECS PHOIBOS150 MCD spectrometer (X-ray source with Mg and Al anodes and Al and Ag monochromatic sources, and 1253.6 eV). Spectra were recorded in constant pass energy mode at 30 eV, using a 720 μm diameter analysis area with charge compensation. Charge referencing was carried out using the adventitious carbon peak (C 1s at 284.8 eV). The CasaXPS version 2.3.16 software package was used for data analysis.

3.6. Electrochemical methods

Electrochemical measurements were performed in a classical three-electrode cell, using a potentiostat/galvanostat (PalmSens4). 0.1 M KOH solution was used as an aqueous electrolyte solution, while Ag/AgCl and graphite rods were used as reference and counter electrodes, respectively. A glassy carbon disk (GCE, 5 mm in diameter, from Pine Research, Ref. AFE3T050GC) was used as a working electrode. Additionally, a rotating ring-disk electrode (RRDE) composed of a glassy carbon-disk with a Au-ring (Ref. AFE6R2GCAU from Pine Research) electrode was employed in a modulated speed rotator (AFMSRCE model from Pine Research).

Both working electrodes were modified with the different as-prepared ZIF-materials by drop-casting a mixture containing 5 μL of Nafion and 20 μL of the ZIF-sample at a concentration of 5 mg mL^{-1}. All potentials were referenced to the reversible hydrogen electrode (RHE) by using the Nernst equation.[16]

3.7. Computational methods

3.7.1 Structure construction. The crystal structure of ZIF-8 was obtained from Huang *et al.*[50] This structure is cubic with a lattice size of 17.012 Å, and the stoichiometry of the unit cell is $C_{96}H_{120}N_{48}Zn_{12}$ (Fig. 4A(1)). From this structure, cut-out surfaces were constructed along the (110) face, with dimensions of 17.012 Å × 24.058 Å and a thickness of 12.029 Å (Fig. 4A(1) and (2)). These cut-out slabs retain the same total volume and stoichiometry as the original cubic framework. The overall structure remains electrically neutral, as any excess positive or negative charge on the upper surface is compensated by an equal and opposite charge on the lower surface.

3.7.2 Density functional theory (DFT) studies. DFT calculations were performed using the DMol3 module implemented in the Materials Studio 2021 software package from Accelrys.[51,52] The positions of the metal, the ligands coordinated to metals, and the adsorbates (O_2, OOH, O, OH and H_2O) were optimized, keeping the positions of the rest of the atoms (C and N) in the unit cell fixed. For this purpose, the generalized gradient approximation parametrized by the revised Perdew–Burke–Ernzerhof (GGA/RPBE) exchange–correlation functional was employed,[53] using dispersion corrections,[54] spin-unrestricted calculations and an accuracy level corresponding to the 4.4 DNP basis set. All electrons were included in the calculations, and the solvation effects were considered using the Conductor-like Screening Model (COSMO).[55,56]

3.8. Batteries

A battery cycler BioLogic BCS-810 was used to perform the galvanostatic discharge analysis of the selected ZIF-materials, specifically the nanosized sample doped with 20% mol Mg ($nZIFMg_{20}$) and it was compared with its non-doped counterpart ($nZIFMg_0$). $nZIFMg_0$, $nZIFMg_{20}$ and 10% wt. Pt–C (from Sigma-Aldrich) were used to prepare the positive electrodes, which were tested in a Zn/KOH/air battery. A 45 μL drop of different samples at a concentration of 15 mg mL^{-1} (*i.e.*, 0.675 mg of catalyst) was mixed with 5 μL of Nafion solution 5% wt. and then loaded drop by drop onto a carbon cloth gas diffusion layer (GDL ELAT LT1400W from Fuel Cells Store). A 6 M KOH aqueous solution as liquid electrolyte with a final volume of 1 mL, and a Zn plate was used as the anode. Nickel mesh was used as the current collector, and the electrode/electrolyte contact area was 0.63 cm^2 in all cases. Galvanostatic discharge curves were recorded at current intensities of −1 and −5 mA.

4. Conclusions

Inspired by the role of Mg as a cofactor in nature, bimetallic Mg-doped ZIF-8 materials with different Mg doping percentages and tuneable particle sizes (nano- or microsizes) were efficiently synthesized using a one-pot simple, reproducible and green method (in water media under atmospheric conditions). On the one hand, we found that nanosized catalysts clearly favoured the ORR electrocatalytic performance, as expected. On the other hand, the incorporation of the Mg ions into the ZIF-structure

drastically improved the ORR response, with the $nZIFMg_{20}$ sample (containing an actual Mg-doping of 14.2 mol%) exhibiting the best ORR electrocatalytic performance following a four-electron pathway and producing a very low percentage of peroxide (<1%). Moreover, durability tests conducted in alkaline electrolyte demonstrated the exceptional stability of $nZIFMg_{20}$, which is a critical factor for its industrial applications. Computational studies revealed that Mg-doping promotes the formation of surface defects on ZIF-8, which greatly decreases the free energies of adsorption for both O_2 and H_2O molecules, facilitating the ORR process.

The outstanding ORR electrocatalytic performance of the $nZIFMg_{20}$ material as a cathode in primary ZABs was investigated, demonstrating not only its better response compared to the pristine ZIF-8 (*i.e.* $nZIFMg_0$) but also its superior performance with respect to the 10% wt. Pt–C standard. Interestingly, this work paves the way to explore other bimetallic approaches in the design of MOF-based catalysts for batteries and other energy storage devices.

Data availability

The data for this article are available in the ZENODO repository at DOI: **https://doi.org/10.5281/zenodo.14380339**, including Dynamic Light Scattering (DLS) particle size distribution analysis, Powder X-ray Diffraction (PXRD) patterns, Inductively Coupled Plasma Optical Emission Spectroscopy (ICP-OES) analysis, N_2 adsorption–desorption isotherms, X-ray Photoelectron (XPS) spectra, ORR electrochemical analysis under static and dynamic conditions (RDE and RRDE), DFT calculations of the free energy adsorption values of the different adsorbates involved in the ORR mechanism and analysis of the best material as the air electrode of a zinc–air battery.

Author contributions

C. C.-C. and M. C. conceived the idea and designed the research; C. C.-C. synthesized and characterized the materials; J. A. S.-D., V. G.-C., M. C., and J. J. G.-C. carried out the electrocatalytic experiments; L. C. performed the theoretical studies; V. G.-C., and A. J. F. R. performed the Zn–air battery tests; C. C.-C. drafted the manuscript. All authors have discussed the results and given approval to the manuscript.

Conflicts of interest

There are no conflicts to declare.

Acknowledgements

The authors would like to acknowledge the financial support from MICIU/AEI/10.13039/501100011033 and FEDER/UE (PID2022-141034OB-C22 project to C.C.-C., PID2022-139191OB-C32 project to A. J. F.-R. and PID2020-112744GB-I00 to J. J. G. C.). V. G.-C. thanks the "Plan Propio de Investigación" from the University of Córdoba for financial support through a predoctoral contract (Submodality 2.2).

References

1 S. V. Venkatesan, A. Nandy, K. Karan, S. R. Larter and V. Thangadurai, *Electrochem. Energy Rev.*, 2022, **5**, 16.
2 R. Sharma, H. Kumar, G. Kumar, S. Sharma, R. Aneja, A. K. Sharma, R. Kumar and P. Kumar, *Chem. Eng. J.*, 2023, **468**, 143706.
3 Y. Chen, Y. Kang, Y. Zhao, L. Wang, J. Liu, Y. Li, Z. Liang, X. He, X. Li, N. Tavajohi and B. Li, *J. Energy Chem.*, 2021, **59**, 83–99.
4 W. Zhang, J. Zhang, N. Wang, K. Zhu, C. Yang, Y. Ai, F. Wang, Y. Tian, Y. Ma, Y. Ma, X. Zhang, L. Duan, D. Chao, F. Wang, D. Zhao and W. Li, *Nat. Sustain.*, 2024, **7**, 463–473.
5 Y. Irmawati, B. Prakoso, F. Balqis, Indriyati, R. Yudianti, F. Iskandar and A. Sumboja, *Energy Fuels*, 2023, **37**, 4858–4877.
6 C. Li, H. Zhang, M. Liu, F. F. Lang, J. Pang and X. H. Bu, *Ind. Chem. Mater.*, 2023, **1**, 9–38.
7 A. Kundu, T. Kuila, N. C. Murmu, P. Samanta and S. Das, *Mater. Horiz.*, 2023, **10**, 745–787.
8 M. Cui, B. Xu, X. Shi, Q. Zhai, Y. Dou, G. Li, Z. Bai, Y. Ding, W. Sun, H. Liuaf and S. Dou, *J. Mater. Chem. A*, 2024, **12**, 18921–18947.
9 N. Cheng, L. Ren, X. Xu, Y. Du and S. X. Dou, *Adv. Energy Mater.*, 2018, **8**, 1801257.
10 Y. Yuan, X. Li, X. Sun, Y. Sun, M. Yang, B. Liu, D. Yang, H. Li and Y. Liu, *Nano Energy*, 2025, **136**, 110727.
11 M. Zhang, H. Mao, Y. Liang and X. Yu, *J. Mater. Chem. A*, 2023, **11**, 17892–17919.
12 Z. Kong, T. Liu, K. Hou and L. Guan, *J. Mater. Chem. A*, 2022, **10**, 2826–2834.
13 J. Jiang, X. L. Zhou, H. G. Lv, H. Q. Yu and Y. Yu, *Adv. Funct. Mater.*, 2023, **33**, 2212160.
14 A. Shahzad, F. Zulfiqar and M. A. Nadeem, *Coord. Chem. Rev.*, 2023, **477**, 214925.
15 C. Wang, J. Kim, J. Tang, M. Kim, H. Lim, V. Malgras, J. You, Q. Xu, J. Li and Y. Yamauchi, *Chem*, 2020, **6**, 19–40.
16 A. Franco, J. Á. Salatti-Dorado, V. García-Caballero, S. Lorca, L. Camacho, M. Cano, A. J. Fernández-Romero, J. J. Delgado, J. J. Giner-Casares and C. Carrillo-Carrión, *J. Mater. Chem. A*, 2022, **10**, 24590–24597.
17 S. Dou, C.-L. Dong, Z. Hu, Y.-C. Huang, J.-l. Chen, L. Tao, D. Yan, D. Chen, S. Shen, S. Chou and S. Wang, *Adv. Funct. Mater.*, 2017, **27**, 1702546.
18 X. He, X. Yi, F. Yin, B. Chen, G. Li and H. Yin, *Electrochim. Acta*, 2020, **337**, 135825.
19 C. Singh, I. Liberman, R. Shimoni, R. Ifraemov and I. Hod, *J. Phys. Chem. Lett.*, 2019, **10**(13), 3630–3636.
20 H. Zhong, K. H. Ly, M. Wang, Y. Krupskaya, X. Han, J. Zhang, J. Zhang, V. Kataev, B. Büchner, I. M. Weidinger, S. Kaskel, P. Liu, M. Chen, R. Dong and X. Feng, *Angew. Chem., Int. Ed.*, 2019, **58**, 10677–10682.
21 S. Liu, Z. Li, C. Wang, W. Tao, M. Huang, M. Zuo, Y. Yang, K. Yang, L. Zhang, S. Chen, P. Xu and Q. Chen, *Nat. Commun.*, 2020, **11**, 938.

22 A. Quintero, J. Racedo and H. Negrete, Electrolytic Abnormalities Related to Magnesium in Critically Ill Cancer Patients, in *Oncologic Critical Care*, ed. J. Nates and K. Price, Springer, Cham, 2019, pp. 1067–1077.
23 J. R. Black, Q.-Z. Yin, J. R. Rustad and W. H. Casey, *J. Am. Chem. Soc.*, 2007, **129**, 8690–8691.
24 S. Horike, K. Kadota, T. Itakura, M. Inukaid and S. Kitagawa, *Dalton Trans.*, 2015, **44**, 15107–15110.
25 Y. Pan, D. Heryadi, F. Zhou, L. Zhao, G. Lestari, H. Sub and Z. Lai, *CrystEngComm*, 2011, **13**, 6937–6940.
26 D. Verdoorn, A. Zuliani, P. Ranjan, J. P. Holgado, N. Khiar, J. M. Saya, C. Carrillo-Carrión, B. U. W. Maes, R. V. Orru and R. V, *Adv. Synth. Catal.*, 2025, e202401540.
27 L. Wang, Z. Wang, L. Xie, L. Zhu and X. Cao, *ACS Appl. Mater. Interfaces*, 2019, **11**, 16619–16628.
28 K. S. Park, Z. Ni, A. P. Côté, J. Y. Choi, R. Huang, F. J. Uribe-Romo, H. K. Chae, M. O'Keeffe and O. M Yaghi, *Proc. Natl. Acad. Sci. U. S. A.*, 2006, **103**, 10186–10191.
29 E. L. Bustamante, J. L. Fernández and J. M. Zamaro, *J. Colloid Interface Sci.*, 2014, **424**, 37–43.
30 M. Jian, B. Liu, R. Liu, J. Qu, H. Wang and X. Zhang, *RSC Adv.*, 2015, **5**, 48433–48441.
31 D. Kim, J. Park, J. Park, J. Jang, M. Han, S.-H. Lim, D. Y. Ryu, J. You, W. Zhu, Y. Yamauchi and J. Kim, *Small Methods*, 2024, **8**, 2400236.
32 S. R. Balestra, B. Martínez-Haya, N. Cruz-Hernández, D. W. Lewis, S. M. Woodley, R. Semino, G. Maurin, A. R. Ruiz-Salvador and S. Hamad, *Nanoscale*, 2023, **15**, 3504–3519.
33 W. Li and Z. Sun, *J. Phys. Chem. Lett.*, 2024, **16**, 503–509.
34 L. Hu, L. Chen, X. Peng, J. Zhang, X. Mo, Y. Liu and Z. Yan, *Microporous Mesoporous Mater.*, 2020, **299**, 110123.
35 A. Schejn, A. Aboulaich, L. Balan, V. Falk, J. Lalevée, G. Medjahdi, L. Aranda, K. Mozeta and R. Schneider, *Catal. Sci. Technol.*, 2015, **5**, 1829–1839.
36 S. Sun, Z. Yang, J. Cao, Y. Wang and W. Xiong, *J. Solid State Chem.*, 2020, **285**, 121219.
37 A. I. A. Soliman, A.-M. A. Abdel-Wahaba and H. N. Abdelhamid, *RSC Adv.*, 2022, **12**, 7075–7084.
38 N. Rani, S. Chahal, S. K. Mahadevan, P. Kumar, R. Shukla and S. K. Singh, *J. Nanotechnol.*, 2020, **31**, 374004.
39 A. Franco, A. Negi, R. Luque and C. Carrillo-Carrión, *ACS Sustainable Chem. Eng.*, 2021, **9**(24), 8090–8096.
40 Z. Jiang, L. Ge, L. Zhuang, M. Li, Z. Wang and Z. Zhu, *ACS Appl. Mater. Interfaces*, 2019, **11**, 44300–44307.
41 L. Tao, C. Y. Lin, S. Dou, S. Feng, D. Chen, D. Liu, J. Huo, Z. Xia and S. Wang, *Nano Energy*, 2017, **41**, 417–425.
42 A. F. Möslein, L. Donà, B. Civalleri and J.-C. Tan, *ACS Appl. Nano Mater.*, 2022, **5**, 6398–6409.
43 J. K. Nørskov, J. Rossmeisl, A. Logadottir, L. Lindqvist, J. R. Kitchin, T. Bligaard and H. Jónsson, *J. Phys. Chem. B*, 2004, **108**, 17886–17892.
44 W. T. Hong, M. Risch, K. A. Stoerzinger, A. Grimaud, J. Suntivich and Y. Shao-Horn, *Energy Environ. Sci.*, 2015, **8**, 1404–1427.
45 I. C. Man, H.-Y. Su, F. Calle-Vallejo, H. A. Hansen, J. I. Martínez, N. G. Inoglu, J. Kitchin, T. F. Jaramillo, J. K. Nørskov and J. Rossmeisl, *ChemCatChem*, 2011, **3**, 1159–1165.
46 D. Fairen-Jimenez, R. Galvelis, A. Torrisi, A. D. Gellan, M. T. Wharmby, P. A. Wright, C. Mellot-Draznieks and T. Düren, *Dalton Trans.*, 2012, **41**, 10752–10762.
47 B. Russell, J. Villaroel, K. Sapag and A. D. Migone, *J. Phys. Chem. C*, 2014, **118**, 28603–28608.
48 J. Ma, J. Li, R. Wang, Y. Yang, P. Yin, J. Mao, T. Ling and S. Qiao, *Mater. Today Energy*, 2021, **19**, 100624.
49 J. Amaro-Gahete, V. García-Caballero, A. Benítez, D. G. Gil-Gavilán, R. Rojas-Luna, D. Esquivel, A. J. Fernández-Romero, M. Cano, J. J. Giner-Casares and F. J. Romero-Salguero, *J. Electroanal. Chem.*, 2023, **948**, 117800.
50 X.-C. Huang, Y.-Y. Lin, J.-P. Zhang and X.-M. Chen, *Angew. Chem., Int. Ed.*, 2006, **45**, 1557–1559.
51 B. Delley, *J. Chem. Phys.*, 2000, **113**, 7756–7764.
52 B. Delley, *J. Chem. Phys.*, 1990, **92**, 508–517.
53 B. Hammer, L. B. Hansen and J. K. Nørskov, *Phys. Rev. B: Condens. Matter Mater. Phys.*, 1999, **59**, 7413.
54 S. Grimme, *J. Comput. Chem.*, 2006, **27**, 1787–1799.
55 A. Klamt and G. Schüürmann, *J. Chem. Soc., Perkin Trans. 2*, 1993, **2**, 799–805.
56 J. Tomasi and M. Persico, *Chem. Rev.*, 1994, **94**, 2027–2094.

